Applying a homogeneous pressure distribution to the upper vertebral endplate: validation of a new loading system, pilot application to human vertebral bodies, and finite element predictions of DIC measured displacements and strains

Massimiliano Baleani[1], Giulia Fraterrigo[2], Paolo Erani[1],
Giulia Rota[1], Matteo Berni[1], Fulvia Taddei[2], Enrico Schileo[2]

[1] IRCCS Istituto Ortopedico Rizzoli, Laboratorio di Tecnologia Medica, Bologna, Italy
[2] IRCCS Istituto Ortopedico Rizzoli, Laboratorio di Bioingegneria Computazionale, Bologna, Italy

CORRESPONDING AUTHOR for all stages of publication:
Massimiliano Baleani
IRCCS Istituto Ortopedico Rizzoli, Laboratorio di Tecnologia Medica
Via Di Barbiano 1/10, 40136 Bologna (BO), ITALY
Tel +39 051 6366865, e-mail: massimiliano.baleani@ior.it

POST-PUBLICATION CORRESPONDENCE TO
Experimental tests: Massimiliano Baleani
IRCCS Istituto Ortopedico Rizzoli, Laboratorio di Tecnologia Medica
Via Di Barbiano 1/10, 40136 Bologna (BO), ITALY
Tel +39 051 6366865, e-mail: massimiliano.baleani@ior.it

Numerical Models: Enrico Schileo
IRCCS Istituto Ortopedico Rizzoli, Laboratorio di Bioingegneria Computazionale
Via Di Barbiano 1/10, 40136 Bologna (BO), ITALY
Tel +39 051 6366554, e-mail: enrico.schileo@ior.it

ABSTRACT

Image-based personalised Finite Element Models (pFEM) could detect alterations in physiological deformation of human vertebral bodies, but their accuracy has been seldom reported. Meaningful validation experiments should allow vertebral endplate deformability and ensure well-controlled boundary conditions. This study aimed to (i) validate a new loading system to apply a homogeneous pressure on the vertebral endplate during vertebral body compression regardless of endplate deformation; (ii) perform a pilot study on human vertebral bodies measuring surface displacements and strains with Digital Image Correlation (DIC); (iii) determine the accuracy of pFEM of the vertebral bodies.

Homogeneous pressure application was achieved by pressurizing a fluid silicone encased in a rubber silicone film acting on the cranial endplate. The loading system was validated by comparing DIC-measured longitudinal strains and lower-end contact pressures, measured on three homogeneous pseudovertebrae of constant transversal section at 2.0 kN, against theoretically calculated values. Longitudinal strains and contact pressures were rather homogeneous, and their mean values close to theoretical calculations (5% underestimation).

DIC measurements of surface longitudinal and circumferential displacements and strains were obtained on three human vertebral bodies at 2.0 kN. Complete displacement and strain maps were achieved for anterolateral aspects with random errors $\leq$0.2 µm and $\leq$30 µstrain, respectively. Venous plexus and double curvatures limited the completeness and accuracy of DIC data in posterior aspects.

pFEM of vertebral bodies, including cortical bone mapping, were built from computed tomography images. In anterolateral aspects, pFEM accuracy of the three vertebrae was: (i) comparable to literature in terms of longitudinal displacements ($R^2>0.8$); (ii) extended to circumferential displacements (pooled data: $R^2>0.9$) and longitudinal strains (zero median error, 95% error: <27%). Circumferential strains were overestimated (median error: 39%).

The new methods presented may permit to study how physiological and pathologic conditions influence the ability of vertebral endplates/bodies to sustain loads.

Keywords:

Spine; Human Vertebrae; Mechanical Testing; Boundary Conditions; Digital Image Correlation, Computed Tomography; Finite Element Models; Validation Experiment

1. INTRODUCTION

Vertebral integrity can be threatened by degenerative or pathological processes. The non-invasive assessment of vertebral biomechanics is usually performed through personalized Finite Element Models (pFEM) built from diagnostic data, in most cases from Computed Tomography (CT). Most pFEM so far focused on the prediction of vertebral strength. Several research groups achieved rather high determination coefficients for pFEM-predicted vs. experimentally measured vertebral strength (R^2 range [0.79 – 0.96]) (Buckley et al., 2007; Choisne et al., 2015; Crawford et al., 2003; Dall'Ara et al., 2010; Imai et al., 2006; Mirzaei et al., 2009; Zeinali et al., 2010). Besides vertebral strength, it would also be important to quantify vertebral strains under physiological loads (for which measurements in different motor activities (Rohlmann et al., 2014, 2013) and validated estimates exist (Bruno et al., 2015)), and understand how these can be modified, or even become alarming, by altered loads (e.g., in reduced gravity conditions) or structural defects (e.g. lytic lesions). Strain validation of vertebral pFEM has been seldom attempted. Apart from some works that using generic vertebral models could not achieve accurate prediction of strains (Ayturk and Puttlitz, 2011; Whyne et al., 2003), a single study reported a detailed validation of a pFEM against strain gauge measurements, reaching a moderate level of accuracy ($R^2 = 0.70$) (Imai et al., 2006).

The experimental setup of Imai et al. applied a vertical load onto vertebrae whose endplates were embedded in endcaps, i.e., acrylic molds including an endplate on the vertebral body on one side and attached to a rigid plate onto which load was applied on the other. This concept of the loading setup is shared by several other validation studies (e.g., Buckley et al., 2007; Chevalier et al., 2008; Choisne et al., 2015; Crawford et al., 2003). Another loading setup consists in removing both vertebral endplates to obtain two parallel flat surfaces so that the load can be applied by rigid plates directly on the vertebral body (Dall'Ara et al., 2010). These two setups are the most common for the mechanical testing of single vertebral bodies, and share two limitations:

(i) by applying a uniform displacement of the whole superior endplate, they neglect that vertebral bodies are complex structures with endplates showing some degree of curvature (Banse et al., 2001; Langrana et al., 2006), which could undergo complex deformation even when axially compressed (Gustafson et al., 2017b; Palanca et al., 2021). In other words, they do not permit the deformation of vertebral endplates, which has been determined as a defining feature of vertebral damage/failure (Jackman et al., 2014). In the case of bone defects or lesions, local effects involving endplate deformation could be critical in defining the vertebral response even to physiological loading regimes, given that already in intact conditions different vertebrae may exhibit different strain patterns when loaded (Hussein et al., 2018);

(ii) the accurate replication in the pFEM of the actual boundary conditions on the vertebra object of measurement is limited by experimental artefacts. In fact, measured loads or displacements are applied to the rigid plate of the loading machine and as such transposed to the pFEM, but a perfect contact at the endplate/acrylic mold or at the vertebral body section/metal plate is almost impossible to achieve. Indeed, end artefacts, due to endplate removal, or narrow gap, due to resin shrinkage, could allow subtle interface micromotions: even an interface gap of few microns alters the strain distribution of the vertebral body and its response to external load (Maquer et al., 2014). A very accurate definition of boundary conditions would instead be required to validate strains, as vertebrae are short and irregular in shape, with shortenings of few microns under load (Hussein et al., 2018).

The limitation about endplate deformability has been overcome experimentally by a third validation setup that performs tests on whole functional spinal units (FSU) (Groenen et al., 2018; Jackman et al., 2016) by leaving in place intervertebral disks. However, when displacements of adjacent intervertebral discs were not measured during the experiment and applied to the pFEM, like in Groenen et al. (2018), it resulted in moderate stiffness and weak failure predictions likely due to uncertainties in the definition of the actual boundary conditions at the vertebral endplates. Another factor limiting the accuracy of Groenen et al. (2018) may have been the lack of comparison with full field measurements, which in another work (on single vertebral bodies) improved stiffness predictions ((Gustafson et al., 2017a), using Digital Image Correlation (DIC)). Both intervertebral disc displacement and full field measurements could be provided by Digital Volume Correlation (DVC) techniques, but DVC cannot be used for clinically viable pFEM yet, as it currently implies stepwise microCT scanning (Hussein et al., 2018).

A possible solution to achieve vertebral endplate deformation under a well-controlled loading condition would be to develop an experimental model where the pressure applied by a testing machine in load-control on the vertebral endplate (i.e. the boundary conditions) can be controlled, and the deformation of the vertebral body (i.e. the benchmark for model prediction) is measured using a separate DIC system. The aim of this study was thus: (i) to validate an experimental procedure to apply a homogeneous pressure field on the vertebral endplate during vertebral body compression testing; (ii) to assess the feasibility of the proposed procedure by performing a pilot study on vertebral bodies; and (iii) to determine the prediction accuracy, in term of surface displacement and strain, of numerical models of the vertebral body compression testing.

2. MATERIALS AND METHODS

2.1. Specimens, imaging, and preliminary specimen preparation

Three human lumbar vertebrae (L3-L5) from the spine of a single donor (male, 60 y) from an international donation program (Science Care Inc., Phoenix, AZ) were used to conduct this study. The vertebral bodies were kept frozen at -20°C between each step of the experiment.

The specimens were first CT imaged (GSI Revolution, GE, US) with clinical settings (120kV, 1.25 mm slice thickness) together with a densitometric phantom (European Spine Phantom, QRM, DE).

Vertebrae were then isolated, and an anatomical reference system was identified on each vertebra according to Panjabi et al. (1992). Vertebral posterior processes were cut. To obtain a flat caudal surface, the caudal endplate was resected parallel to the bisector plane of the two endplates.

Aluminum spheres, 1 mm in diameter, were glued on each specimen (six per vertebra, one pair for each monitored aspect), and CT imaging was repeated, to permit the registration of the experimental and pFEM reference systems.

The external contour of the cranial endplate of each vertebra, obtained from the segmentation of the CT images (Section 2.3.2.), was projected onto the horizontal plane of the vertebra, and served as input to machine L3-L5 pseudovertebrae (hereinafter PL3-PL5) from a bulk of ultra-high molecular weight polyethylene (UHMWPE). Thus, pseudovertebrae had the cranial endplate replicating the 3D shape of the cranial vertebral endplate, but vertically straight lateral walls, i.e., constant cross section. The UHMWPE had a compressive elastic modulus E=1.84±0.03 GPa as experimentally determined through compression testing, performed at 20 °C, of three cylindrical specimens (height 50 mm, heigh/diameter ratio of 3:1) extracted from the same 50 mm thick UHMWPE sheet used to machine the pseudovertebrae.

The three pseudovertebrae, being homogeneous and elastic, were used to validate the experimental setup, assuming a Poisson's ratio ν=0.46 (Sherazi, 2014), and then modelled to ensure that the experimentally applied boundary conditions were accurately replicated in the FE models. The three human vertebrae were then used to obtain pilot experimental data and validate the FE modelling procedure in terms of displacements and strain prediction.

2.2. Experiments

2.2.1. Loading System

To achieve a homogeneous pressure on the vertebral cranial endplate, we designed a loading device that (i) had the negative shape of the endplate, to ensure contact over the entire endplate surface and (ii) was flexible enough to follow endplate deformation without altering the pressure distribution over the endplate. We realized this concept by applying load through a fluid silicone encased in a

thin film of rubber silicone directly molded onto the vertebral endplate. To avoid bulging, the film was fully constrained except for the areas in contact with the vertebral endplate and the actuator end. A scheme of the proposed loading system is reported in Figure 1. Details are reported in Appendix A.

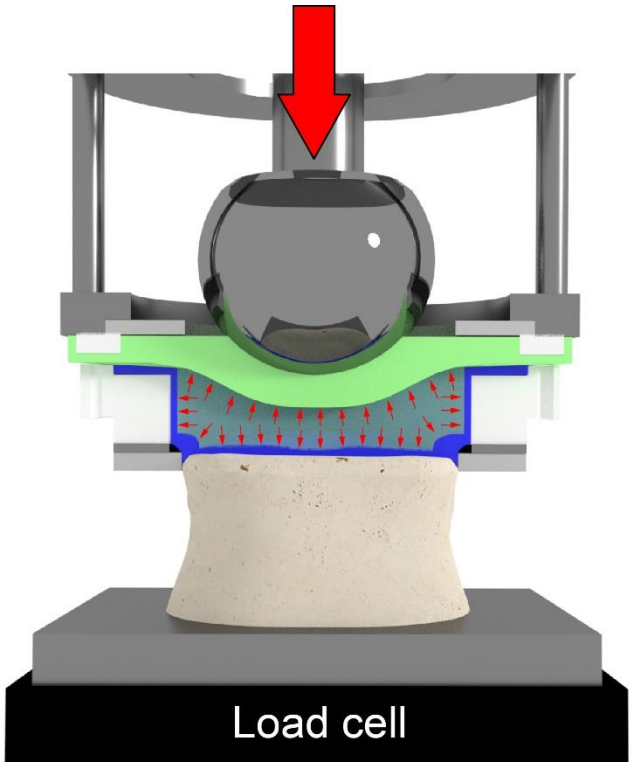

Figure 1: Schematic of the loading system. The compressive load is applied to the cranial endplate through a fluid silicone encased in a thin silicone rubber film. Details are reported in Appendix A.

2.1.2. Experimental tests

Specimen Preparation

Stochastic pattern was created on the walls of each pseudovertebra or vertebra (hereinafter specimen, unless it is necessary to specify them) by covering the surface with water based white paint and then airbrushing acrylic black paint (details in Acciaioli et al. (2020)) to achieve speckle dimensions in the recommended range of 3-5 pixels (Lionello and Cristofolini, 2014; Schreier et al., 2009; Zhou, 2001). Surface finish of the lower flat surface was obtained by gentle manual sanding, first with a 100 grit, then with a 400 grit sandpaper.

Loading Protocol

Each specimen was placed on a polished ceramic plate fixed to the load cell (5kN Instron 2518-103, Instron, Norwood, MA) of a material testing machine (Instron 8502, Instron, Norwood, MA). To map the pressure distribution, a pressure sensor array (5076-350, squared 83.8 mm array, Tekscan, Norwood, MA) with sensor size of 1.9 mm in both directions was placed between the lower flat

surface of the pseudovertebra and the ceramic plate. The loading system was lowered vertically to fit the inner contoured aluminum sheet onto the upper specimen endplate (Figure 1), adjusted vertically to apply a preload of about -0.1 kN and locked. The actuator, equipped with 46mm metal hemisphere, was manually lowered to increase the preload to -0.2 kN.

The specimen underwent monotonic compressive test in load control to -2.0 kN, at a rate of 0.1 kN/s, holding the -0.2 kN and -2.0 kN load level for one second. The maximum load was chosen to approximately match the maximum compressive load estimated for demanding daily motor tasks (Bruno et al., 2017).

Data Acquisition

Pressure maps were recorded at 15 Hz during the test. Simultaneously, the two cameras of a DIC system (Aramis 5M, GOM Metrology GmbH, Braunschweig, Germany) monitored one aspect of the specimen to measure the surface displacement at 15 Hz.

The DIC system was calibrated using a 15x12 mm panel. The nominal visible area was 27.0x22.6 mm, determining an isotropic pixel of about 11 µm. However, due to height and circumferential curvature limitations of the specimens, the area of interest for displacement and strain measurements was limited to 1332x1332 pixels (about 15x15 mm). This area was centered horizontally in the stereoscopic image focus and started longitudinally from the caudal specimen end. The longitudinal dimension could be further limited by the height of the lateral surface appearing sharp and well illuminated.

Each specimen underwent three test series, to monitor with DIC the right anterolateral, left anterolateral and posterior aspects. Between each series: (i) the loading system and the specimen were rotated by 90° and 135° respectively; (ii) the DIC system was repositioned horizontally to achieve sharp focus. Each series consisted of five test repetitions. To include any bias due to manual specimen sanding, between each test repetition pseudovertebrae were removed from the ceramic plate, gently sanded in a random pattern with 400 grit sandpaper, and repositioned. Each manual sanding was performed by a different operator to capture the variability in pseudovertebra sanding. The vertebra underwent the same procedure except for manual sanding between test repetition to avoid pattern damage close to the caudal end.

2.1.3. Experimental Data Processing

Pressure Maps

Data processing was aimed at comparing the maps of pressure distribution between series. A single mean pressure map for each series was computed by: (i) averaging for each repetition the 15 maps acquired while maintaining for 1 s the load level at -2.0 kN; (ii) averaging again over the five

repetitions. A contour-match algorithm (MATLAB 2020a, The MathWorks, Inc., Natick, MA) allowed in-plane registration of the three mean pressure maps. Relative distances among specific features (if any) of the pressure distribution were calculated to check the test repeatability. To validate pressure measurements, pressure maps achieved testing the pseudovertebrae were compared with the theoretically calculated pressure value (i.e. the ratio between the applied load and the known area of the lower end surface).

DIC Maps

Data processing was aimed at obtaining for each series a mean map, with associated data scattering, for measured displacements and strains.

Captured images were processed using a subset size of 36x36 pixels (about 0.40x0.40 mm), step of 36 pixels (i.e. no subset overlap), and an 11x11 strain window (about 4.36x4.36 mm). These values were experimentally determined for a single image captured on all vertebral aspects, following the three-factor approach described in Acciaioli et al. (2018). For each repetition of each series, a mean differential displacement map was computed from the 15 maps recorded at -0.2 kN (reference level) and -2.0 kN (maximum load). Table 1 reports measurements precision in terms of mean (systematic error) and standard deviation (random error) of displacement and strain values (Palanca et al., 2015) measured at the reference load value of -0.2 kN in load control for two seconds (note: the first second was necessary to acquire 15 maps defining the reference map, the subsequent second was necessary to acquire 15 maps used to calculate errors).

Table 1: Results of the zero displacement and strain test. Mean (systematic error) and standard deviation (random error) of measured displacement and strain values. Strain values are rounded up to the nearest tenth.

LONGITUDINAL DISPLACEMENT						
Vertebra	*Right Anterolateral aspect*		*Left Anterolateral aspect*		*Posterior aspect*	
	Mean (systematic error) [µm]	SD (random error) [µm]	Mean (systematic error) [µm]	SD (random error) [µm]	Mean (systematic error) [µm]	SD (random error) [µm]
L3	< -0.1	< 0.1	< -0.1	< 0.1	-0.1	0.1
L4	< -0.1	< 0.1	< -0.1	< 0.1	-0.1	0.1
L5	< -0.1	< 0.1	< -0.1	< 0.1	< -0.1	0.1
CIRCUMFERENTIAL DISPLACEMENT						
Vertebra	*Right Anterolateral aspect*		*Left Anterolateral aspect*		*Posterior aspect*	
	Mean (systematic error) [µm]	SD (random error) [µm]	Mean (systematic error) [µm]	SD (random error) [µm]	Mean (systematic error) [µm]	SD (random error) [µm]
L3	< |0.1|	0.2	< |0.1|	0.2	0.1	0.4
L4	< |0.1|	0.2	< |0.1|	0.1	-0.1	0.4
L5	< |0.1|	0.1	0.1	0.2	0.1	0.3
LONGITUDINAL STRAIN						
Vertebra	*Right anterolateral aspect*		*Left anterolateral aspect*		*Posterior aspect*	
	Mean (systematic error) [µstrain]	SD (random error) [µstrain]	Mean (systematic error) [µstrain]	SD (random error) [µstrain]	Mean (systematic error) [µstrain]	SD (random error) [µstrain]
L3	< -10	10	< -10	10	< -10	50
L4	< -10	10	< -10	10	< -10	40
L5	< -10	10	< -10	10	< -10	40
CIRCUMFERENTIAL STRAIN						
Vertebra	*Right anterolateral aspect*		*Left anterolateral aspect*		*Posterior aspect*	
	Mean (systematic error) [µstrain]	SD (random error) [µstrain]	Mean (systematic error) [µstrain]	SD (random error) [µstrain]	Mean (systematic error) [µstrain]	SD (random error) [µstrain]
L3	< 10	20	< 10	30	10	80
L4	< 10	30	< 10	20	10	60
L5	< 10	20	< 10	20	10	60

The five displacement/strain maps per series were spatially registered using a reference system placed in a clearly identifiable point on the pattern, located at the caudal end of each specimen and horizontally centered in the stereoscopic image. Mean and standard deviation of displacement and

strain were calculated for the five test repetitions to obtain a single map of measurement/scatter for each aspect. Locations for which values from less than three repetitions were available were discarded.

The mean longitudinal strain measured on the three aspects of the pseudovertebrae was compared with the theoretically calculated longitudinal strain, i.e. the ratio between the differential applied load (-1.8 kN) and the cross-sectional area of the pseudovertebra divided by UHMWPE elastic modulus. The mean circumferential strain, measured on the three aspects of the pseudovertebrae, was compared with the theoretically calculated circumferential strain value, i.e. the theoretically calculated longitudinal strain value multiplied by UHMWPE Poisson's ratio. All analyses were carried out neglecting the first 5 mm surface measured starting from the flat end of the pseudovertebra/vertebra to limit the effect of possible artefacts due to non-ideal contact with the ceramic plate.

2.3. Personalized Finite Element Modelling

2.3.1. Pseudovertebrae

Virtual models of pseudovertebrae (obtained by extruding caudally the surface of the upper endplate) were meshed with 10-node tetrahedral elements (average edge length of 1 mm) and assigned isotropic and homogeneous material properties (E=1.84 GPa, v=0.46, Section 2.1).

2.3.2. Human Vertebrae

From CT images to pFEM including a specimen-specific cortical bone layer

Considering (i) the unavoidable blur that affects the CT representation of cortical walls and endplates, (ii) the significant contribution of cortical bone compartment to overall vertebral mechanics (Eswaran et al., 2006), and (iii) the prospective use of pFEM to study vertebrae affected by lytic lesions, where the cortex may act as a boundary, we chose to include a specimen-specific estimate of the cortical bone layer in the models. Local cortical density and thickness were estimated from CT images by way of a deconvolution algorithm (Cortical Bone Mapping, CBM-v2) (Treece and Gee, 2015).

The procedure to include CBM algorithm in the FE models was adapted from the one developed for the femur (Schileo et al., 2020). Briefly, CT images of each vertebra were segmented through simple grey level thresholding followed by manual adjustment to close contours and exclude posterior elements or osteophytes, obtaining a first estimate of the external contour. On this contour, CBM was run to estimate cortical density, then cortical thickness, and finally reconstruct

triangulated periosteal and endosteal cortical surfaces using medium smoothing level in the CBM free software (Stradview version 6.1, University of Cambridge, UK).

A B-spline representation of the cortical surfaces was obtained (v.7, Raindrop Geomagic, Inc., USA), and clipped caudally to replicate the planar surface obtained on the experimental specimens (Figure 2).

A 10-node tetrahedral mesh was generated both for cortical (average element edge length 0.75 mm, compatible with the average cortical thickness) and trabecular compartments (element edge length 0.75 mm at cortical interface and extending to 2 mm inwards) (Hypermesh v.17.0, Altair Engineering Inc., USA).

Material properties mapping

CT data were density-calibrated with the ESP phantom. The radiological density was converted to ρ_{ash}, and ρ_{ash} was related to apparent density with the ratio $\rho_{ash}/\rho_{app}=0.6$ (Schileo et al., 2008). Bone material properties were assigned to each mesh element based on the density-elasticity relationship derived from vertebral specimens by Ouyang et al. (1997) (Table 2); the same relationship was used both for cortical and trabecular bone, as in Gustafson et al. (2017a).

In the trabecular compartment, inhomogeneous material properties were assigned using the Bonemat algorithm (freeware at www.bonemat.org), that performs on each finite element a numerical integration of voxel-wise properties extracted from the CT images. An upper threshold was applied to the resulting elemental density (and thus Young's modulus), to avoid the possible double-counting of cortical-like density due to the residual blur affecting the data close to the cortical layer. This threshold was set to the maximum value of trabecular bone density tested in the study of Ouyang et al. (1997) from which the density-elasticity relationship was taken (max $\rho_{app}=0.7$ g/cm^3, corresponding to E=1.22 GPa).

In the cortical layer, inhomogeneous material properties were assigned using a specialized Bonemat version (described in Schileo et al. (2020), freeware at www.bonemat.org), which uses as input the local density estimates obtained by Stradwin at surface nodes to perform the numerical integration over each finite element. The resulting density (and Young's moduli) of cortical elements were filtered to exclude possible outliers generated by the non-linear optimization of the CBM-v2 algorithm; we set a lower threshold equal to the upper threshold for the trabecular compartment and an upper threshold determined for each specimen from the maximum HU value found in regions of thick bone cortex that should not be affected by partial volume effects.

Similarly to Crawford et al. (2003), Zeinali et al. (2010), and further motivated by the aim to validate displacements and strains also along the circumferential (x) direction, we modelled both trabecular and cortical bone as transversely isotropic (Table 2). In accordance with the experimental

report from which we adopted the density-elasticity relationship, the Young's moduli obtained from the HU values were considered to be the longitudinal (y) elastic moduli values (E_{long}). In lack of microstructural data, the other engineering constants for trabecular bone, were extracted from literature (Ulrich et al., 1999), as in other research works (Crawford et al., 2003; Zeinali et al., 2010). For cortical bone, in absence of tests performed on vertebral cortex bone, the constants were calculated using anisotropy ratios obtained from experimental tests carried out on femoral cortical bone (Dong and Guo, 2006; Dong and Guo, 2004).

Table 2: Details of transversely isotropic material properties relationships. The longitudinal direction (y) is taken as the principal material direction. Transversal properties are then derived assuming the ratios from literature: (1) Ouyang et al. (1997), (2) Ulrich et al. (1999), (3) Dong and Guo (2004) and (4) Dong and Guo, (2006). Elastic moduli are expressed in GPa.

TRABECULAR BONE	**CORTICAL BONE**
$E_{long} = 2.383\ \rho_{app}^{1.88}$ (1)	$E_{long} = 2.383\ \rho_{app}^{1.88}$ (1)
$E_{circ} = E_{rad} = 0.333\ E_{long}$ (2)	$E_{circ} = E_{rad} = 0.588\ E_{long}$ (3)
$G_{long} = 0.121\ E_{long}$ (2)	$G_{long} = 0.200\ E_{long}$ (3)
$G_{circ} = G_{rad} = 0.157\ E_{long}$ (2)	$G_{circ} = G_{rad} = 0.286\ E_{long}$ (3)
$\nu_{long} = 0.38$ (2)	$\nu_{long} = 0.30$ (4)
$\nu_{circ} = \nu_{rad} = 0.10$ (2)	$\nu_{circ} = \nu_{rad} = 0.40$ (4)

Boundary conditions

The applied boundary conditions were common to pseudovertebrae and vertebrae. All the nodes of the caudal plane were constrained in the longitudinal direction. A ring of six nodes, selected around the center of gravity of the same surface, was constrained also in the other two horizontal directions to permit the model expansion by Poisson effect, but at the same time avoid model lability in the implicit FE formulation. A compressive force of 1.8 kN was uniformly distributed to the superior endplate to replicate the idealized experimental loading condition. Spatial registration of the FE model to the experimental reference system is depicted in Figure 2. The models were solved in ANSYS APDL (Ansys Inc., v. 15, USA).

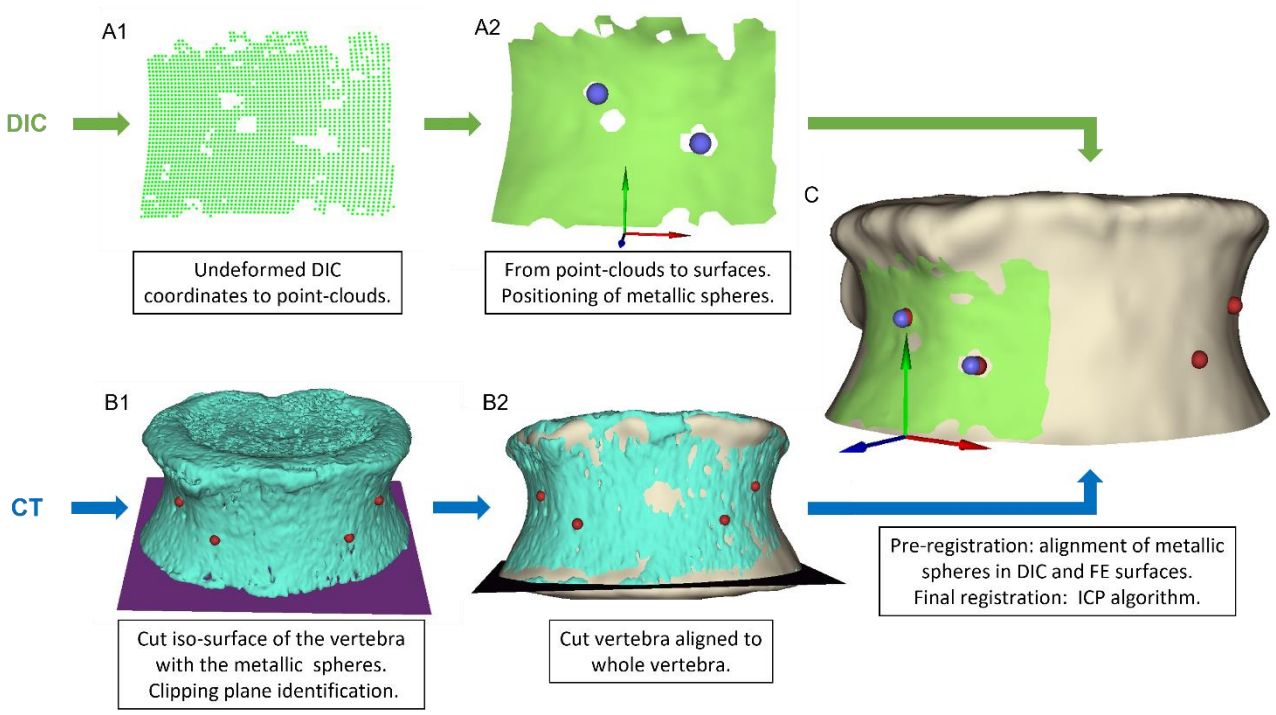

Figure 2: A1) Undeformed DIC coordinates to point-clouds (MATLAB); A2) Conversion of point-clouds into triangulated surfaces (Ball Pivot Algorithm in MeshLab) (Cignoni et al., 2008) and positioning of the metallic spheres; B1) Extraction of iso-surface from CT of the caudal clipping plane; B2) Alignment of the cut vertebra with the clipping plane on the whole vertebra; C) Match of the metallic sphere coordinates in DIC and FE surfaces using Alba (https://github.com/IOR-BIC/ALBA). Run of an iterative closest point (ICP) algorithm to fine tune the registration of the DIC surfaces on each clipped vertebral model (average registration error was 0.17 mm).

2.4. Validation and Statistical Analysis

To obtain a point-wise match between pFEM and DIC data, we developed a code (MATLAB) that for each DIC point averaged the pFEM results over a spherical volume of interest (VOI), with a radius of 0.8 mm, coherently to Grassi et al. (2013). This match was established both for displacement, and strain results.

In pseudovertebrae, DIC to pFEM comparisons were limited to displacements in the longitudinal direction, to ensure (using a homogeneous medium with known elastic modulus) that the boundary conditions of the pFEM could correctly replicate those of the experiment. In vertebral specimens, we validated pFEM predictions of displacement and strain in the longitudinal and circumferential direction.

DIC and pFEM displacements were compared through linear regression analysis, reporting results in term of coefficient of determination (R^2) and slope of the regression line. DIC and pFEM strains were compared through error metrics, reporting point-wise differences as plots of the frequency and spatial distribution of errors.

3. RESULTS

3.1. Validation of the experimental model

3.1.1. Pressure maps

Three representative pressure maps were obtained for each pseudovertebra. The pressure distribution was quite homogeneous over the whole pseudovertebra/ceramic plate interface regardless of pseudovertebra orientation or cross-sectional dimension (Supplementary Material, Appendix B). The mean pressure value (p_{mean}), measured over the real lower end area of each pseudovertebra was close to the theoretically calculated mean pressure value, with a systematic underestimation of 3-6% (Table 3).

Table 3: Comparison between theoretically calculated and experimentally measured mean pressure values (p_{mean}). Percentage errors were calculated with respect to the theoretically calculated value.

Specimen	Calculated p_{mean} [MPa]	*Right anterolateral aspect*		*Left anterolateral aspect*		*Posterior aspect*	
		Measured p_{mean} [MPa]	Percentage error [%]	Measured p_{mean} [MPa]	Percentage error [%]	Measured p_{mean} [MPa]	Percentage error [%]
PL3	1.39	1.34	-4	1.33	-4	1.31	-6
PL4	1.36	1.29	-5	1.28	-6	1.29	-5
PL5	1.34	1.28	-4	1.30	-3	1.29	-4

3.1.2. Displacements

Map vertical dimension was limited to about 14 mm for PL4 and 12 mm for PL5. All maps of longitudinal and circumferential displacements showed quite regular horizontal and vertical bands, respectively (Figure 3). The longitudinal displacement each surface point travelled was roughly proportional to the distance from the lower surface of the pseudovertebra, up to about 10 µm measured on PL3. The circumferential displacements increased quite symmetrically from midline to lateral borders, up to about 3 µm.

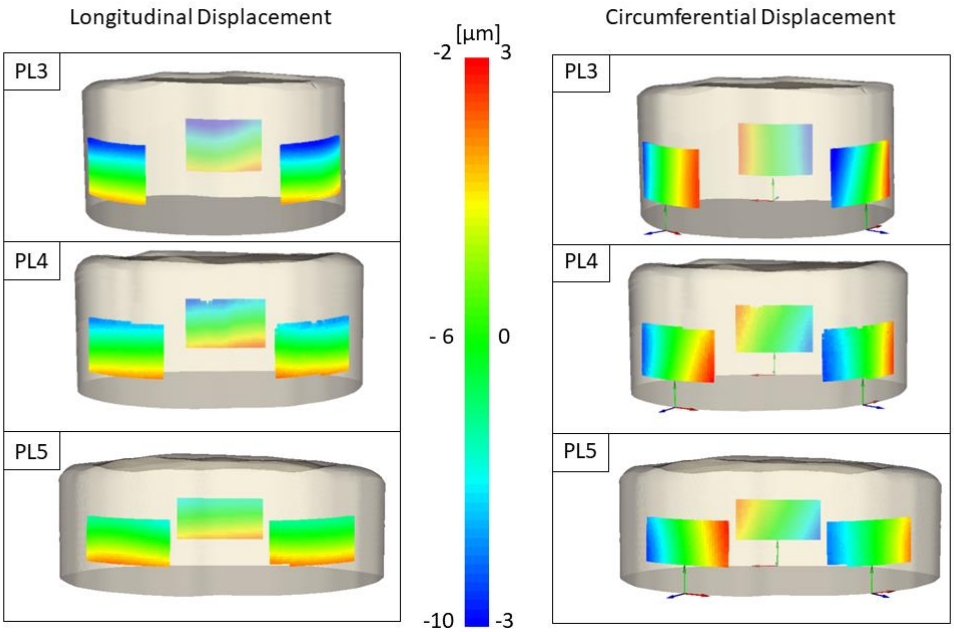

Figure 3: Maps of DIC measured longitudinal (left) and circumferential (right) displacements in pseudovertebrae.

3.1.3. Strain

Longitudinal and circumferential strain level fell within the range [-500, -700] µstrain and [200, 400] µstrain respectively (Figure 4). The mean values of longitudinal strains, calculated for each of the three pseudovertebral aspects, were always comparable (maximum difference of 30 µstrain between right anterolateral and posterior aspect of PL3). The mean values of the longitudinal strains were close to, but systematically smaller than the theoretically calculated values (mean: -5%; range [-8%, -3%]). The mean values of the circumferential strain were, on average, overestimated by 9%, with a larger error range [-13%, + 23%] (Table 4). The range of percentage errors was wider when considering the single test repetitions: [-17%, 6%] for longitudinal strains, [-20%, 29%] for circumferential strains.

Table 4: Comparison between theoretically calculated and experimentally measured longitudinal mean strain value ε_l and circumferential mean strain value ε_c (overall mean value, with minimum and maximum mean values achieved in the five test repetitions in brackets). All strain values were rounded to the nearest ten.

Specimen	Calculated ε_l [µstrain]	*Right Anterolateral aspect*		*Left Anterolateral aspect*		*Posterior aspect*	
		Measured ε_l Mean [range] [µstrain]	Percentage error Mean [range] [%]	Measured ε_l Mean [range] [µstrain]	Percentage error Mean [range] [%]	Measured ε_l Mean [range] [µstrain]	Percentage error Mean [range] [%]
\PL3	-680	-630 [-600, -670]	-7 [-12, -1]	-640 [-610, -660]	-6 [-10, -3]	-660 [-620, -710]	-3 [-9, 4]
PL4	-660	-610 [-570, -660]	-8 [-14, 0]	-620 [-570, -680]	-6 [-14, 3]	-620 [-590, -660]	-6 [-11, 0]
PL5	-650	-620 [-540, -690]	-5% [-17, 6]	-630 [-600, -670]	-3% [-8, 3]	-630 [-550, -690]	-3% [-15, 6]
	Calculated ε_c [µstrain]	Measured ε_c Mean [range] [µstrain]	Percentage error Mean [range] [%]	Measured ε_c Mean [range] [µstrain]	Percentage error Mean [range] [%]	Measured ε_c Mean [range] [µstrain]	Percentage error Mean [range] [%]
PL3	310	350 [330, 360]	13 [6, 16]	380 [360, 400]	23 [16, 29]	360 [350, 370]	16 [13,19]
PL4	300	340 [330, 360]	13 [10, 20]	340 [320, 360]	13 [7, 20]	260 [240, 280]	-13 [-20, 7]
PL5	300	360 [330, 370]	20 [10, 23]	300 [280, 320]	0 [-7, 7]	270 [250, 290]	-10 [-17, -3]

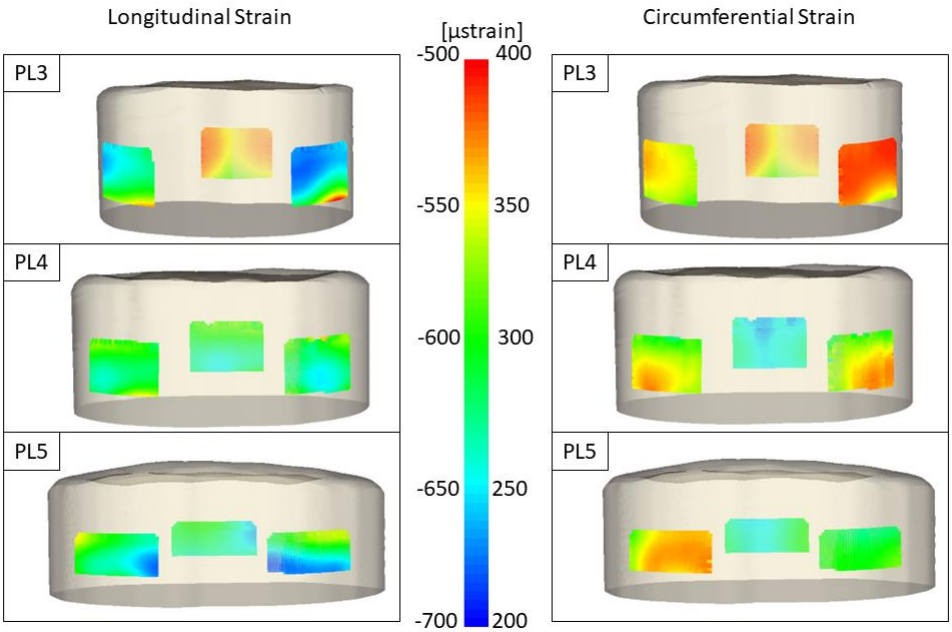

Figure 4: Maps of DIC computed longitudinal (left) and circumferential (right) strains in pseudovertebrae

3.2. Pilot trial on human vertebral bodies

3.2.1. Pressure maps

Three representative pressure maps were obtained for each vertebra. The pressure distribution was not homogeneous, with pressure values increasing from the anterior towards the posterolateral area, the pressure gradient depending on cortical wall thickness. However, pressure peaks, which caused local sensor saturation, were always located posteriorly under the two stumps of the pedicles (Supplementary Material, Appendix B). Test repeatability was confirmed by corresponding pressure peaks, measured in the three series performed on each vertebra, being at most one sensor array row or column apart.

3.2.2. Displacements

The vertical dimension of the maps was limited to about 14 mm for L4 and 12 mm for L5. However, the size of the DIC correlated area was smaller than the monitored surface due to local high three-dimensional curvature, surface discontinuities or gaps (Table 5).

Table 5: Coverage of the DIC correlated area expressed as a percentage of the monitored surface. Values are reported for the subsets used to measure displacements, and are valid also for strain window correlation, except for the posterior aspects, where strain window correlations were further reduced to the values shown in brackets due to the discontinuity of displacement maps.

Vertebra	**CORRELATED AREA**		
	Right Anterolateral aspect [%]	*Left Anterolateral aspect [%]*	*Posterior aspect [%]*
L3	90.4	95.8	26.3 (13.0)
L4	85.2	87.8	51.7 (27.6)
L5	87.8	97.9	71.8 (60.1)

Although roughly horizontal bands for longitudinal displacements could be observed on anterior vertebral aspects, the inter-aspect longitudinal displacements were less homogeneous than those measured in pseudovertebrae.

The largest longitudinal displacements were measured on the posterior aspect of L3 (about -29 µm just above the posterior structural discontinuity) and on the right anterolateral aspect of L4 (about -22 µm), where the maximum gradient in longitudinal displacement (about 7 µm) of surface points lying on the same horizontal level was found. L5 showed the most homogeneous longitudinal displacement distribution: the three longitudinal displacement maps were the most comparable with longitudinal displacement values falling in the range [-4, -15] µm (Figure 5).

Most circumferential displacements fell within the range [-4, 4] µm. However, a roughly symmetrical displacement map (i.e. showing vertical bands) was measured only on L3 anterior

aspects. A similar trend was found on the posterior aspect of L5, although less than 10 percent of the circumferential displacements were outside the range [-2, 2] µm, while discontinuities in the posterior aspects of L3 and L4 did not allow any assessment.

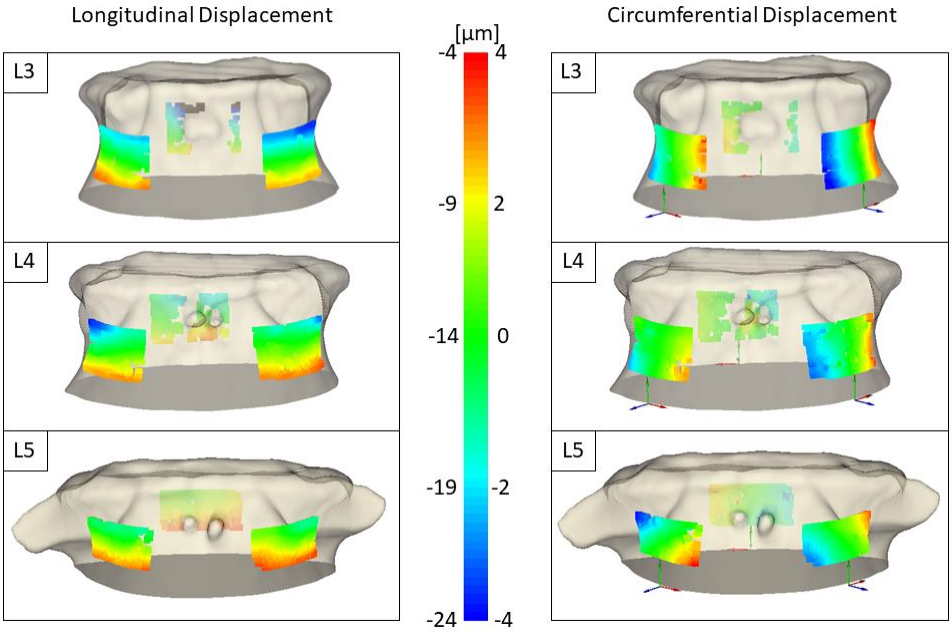

Figure 5: Maps of DIC measured longitudinal (left) and circumferential (right) displacements in human vertebrae. A few outliers exceeding minimum longitudinal displacement in L3 posterior aspect are shown in black.

Strains

Longitudinal and circumferential strain levels fell within the range [-300, -2300] µstrain and [0, 800] µstrain, respectively. The mean longitudinal strain values for L3, L4 and L5 were -1260 µstrain, -1190 µstrain and -1050 µstrain, respectively. The inter-aspect differences were larger than those found testing pseudovetrebrae. The maximum differences in mean strain values among aspects were 210 µstrain, 230 µstrain and 170 µstrain for L3, L4 and L5 respectively. The mean circumferential strain values for L3, L4 and L5 were 380 µstrain, 320 µstrain and 260 µstrain, respectively.

Table 6: Mean longitudinal strains measured on three aspects of each vertebra. Fifth and ninety-fifth percentile of the strain distribution are also reported in brackets.

LONGITUDINAL STRAIN			
Vertebra	*Right Anterolateral aspect*	*Left Anterolateral aspect*	*Posterior aspect*
	Mean [5%, 95 %] [µstrain]	Mean [5%, 95 %] [µstrain]	Mean [5%, 95 %] [µstrain]
L3	-1130 [-1330, -760]	-1320 [-1610, -960]	-1300 [-2060, -1050]
L4	-1220 [-1850, -770]	-1280 [-1780, -1030]	-1040 [-1540, -660]
L5	-1100 [-1220, -950]	-1100 [-1390, -790]	-1020 [-1510, -400]
CIRCUMFERENTIAL STRAIN			
Vertebra	*Right Anterolateral aspect*	*Left Anterolateral aspect*	*Posterior aspect*
	Mean [5%, 95 %] [µstrain]	Mean [5%, 95 %] [µstrain]	Mean [5%, 95 %] [µstrain]
L3	320 [230, 450]	510 [390, 610]	290 [190, 560]
L4	290 [150, 390]	420 [320, 590]	230 [130, 330]
L5	290 [220, 410]	210 [60, 310]	250 [140, 460]

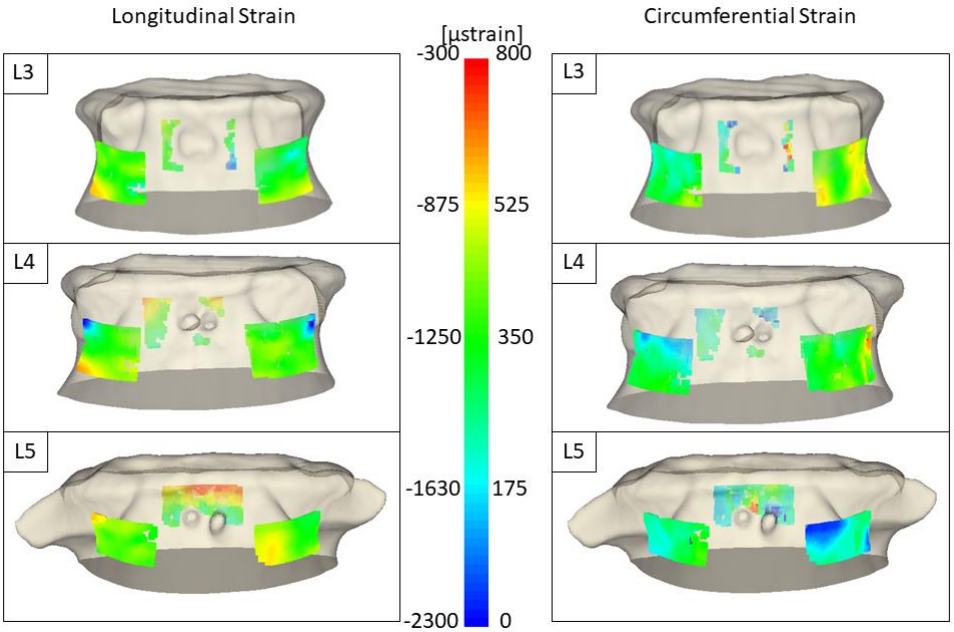

Figure 6: Maps of DIC computed longitudinal (left) and circumferential (right) strains in human vertebrae.

3.3. Accuracy of pFEM estimates against DIC measurements

3.3.1. Pseudovertebrae

Vertical Displacement Validation

The regression analysis on displacement data from all specimens (PL3-PL5) returned a high determination coefficient R^2 (0.94) and a slope of the regression line of 1.01. Values close to ideal matching of experimental and numerical data were obtained also pooling results by specimen, with R^2 ranging [0.92, 0.95] and slope [0.97, 1.02]. Data from single aspects showed slightly higher scatter for slope [0.90, 1.11] but not for R^2 [0.96, 1.00], except for PL3 posterior aspect (0.92) (Table 7).

Table 7: Validation of pFEM longitudinal displacements against DIC measurements in pseudovertebrae.

LONGITUDINAL DISPLACEMENT VALIDATION (PSEUDOVERTEBRAE)										
Pseudovertebra	*Right Anterolateral aspect*		*Left Anterolateral aspect*		*Posterior aspect*		*Pooled by Specimen*		*Total*	
	Slope	R^2	Slope	R^2	Slope	R^2	Slope	R^2	Slope	R^2
PL3	1.06	0.99	1.11	1.00	0.89	0.92	1.00	0.92	1.01	0.94
PL4	1.10	0.97	1.06	0.99	0.94	0.96	1.02	0.95		
PL5	1.03	0.98	1.01	0.96	0.90	0.99	0.97	0.92		

3.3.2. Vertebrae

Validation results in human vertebrae are here reported only for DIC measurements in the two anterior aspects. In these aspects, (i) consistent and continuous DIC field data were available both for displacements and strains, and (ii) the pFEM could robustly reconstruct the bone shape and appearance. Conversely, in the posterior aspect: (i) the presence of high three-dimensional curvature, surface discontinuities or gaps impaired the consistency of DIC acquisitions, so that fewer data were available, down to 26% of the area for displacements and 13% for strains in L3 (Table 5); (ii) the identification of bone boundaries (and thus the distribution and gradients of material properties) in pFEM was uncertain due to the presence of the venous plexus resulting in a sort of irregular cavity. As a result, consistent correlations between pFEM estimates and experimental measurements could be established only for little portions of the DIC acquisition windows and were not considered robust enough to be reported. All comparisons between DIC and pFEM data in posterior aspects are anyway available for completeness (Supplementary Material, Appendices C and D).

Displacement validation

The comprehensive regression of pFEM vs experimental displacements (pooling vertical and circumferential data, supported by non-significant Wilcoxon signed rank test values on residuals, p

> 0.29) returned a determination coefficient of 0.96 and a slope of 1.15 (Figure 7). When separating data into vertical and circumferential displacements, R^2 was still rather high (vertical: 0.84; circumferential: 0.83), and slopes not dissimilar from the overall regression (vertical: 1.18; circumferential: 1.30).

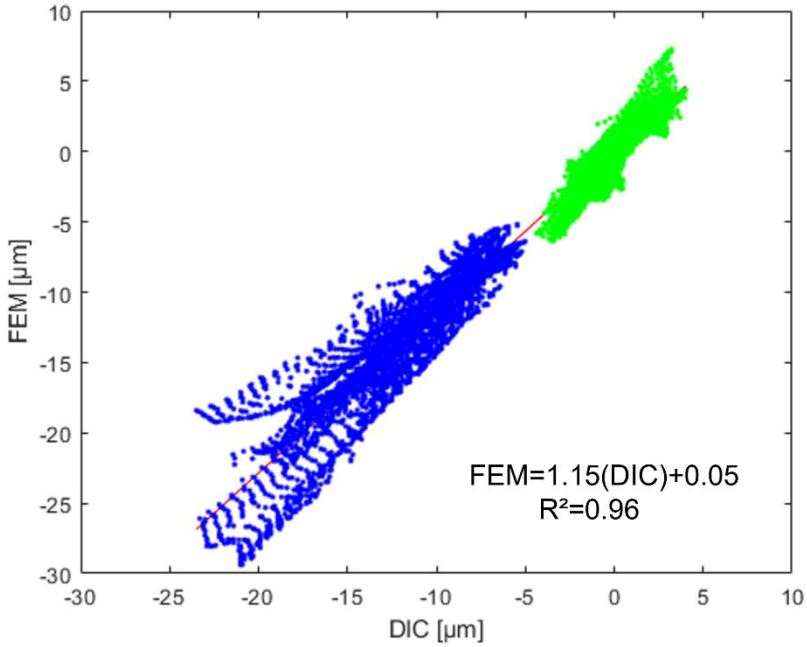

Figure 7: Comprehensive regression plot of experimental (DIC- x axis) and numerical (pFEM – y axis) data from all vertebrae (L3-L5). Vertical displacements in blue, circumferential in green.

When looking at each vertebral aspect separately, some clearer differences emerged, mostly between the vertical and circumferential directions (Table 8). In vertical direction, the R2 was always over 0.91, except in L5 right anterior aspect, and the slope values ranged from 0.85 to 1.28. Regression of circumferential data showed a slightly higher scatter, with a R2 range [0.76, 0.96] (mean R2 = 0.84). Regression slopes were in the range [1.15, 1.42] apart from an outlier (1.78) in the right anterior aspect of L4. Notably, this was the same aspect where the lowest slope value for longitudinal displacements had been observed.

Table 8: Validation of pFEM displacements against DIC measurements in human vertebrae.

LONGITUDINAL DISPLACEMENT VALIDATION (VERTEBRAE)								
Vertebra	*Right Anterolateral aspect*		*Left Anterolateral aspect*		*Pooled by specimen*		*Total*	
	slope	R^2	slope	R^2	slope	R^2	slope	R^2
L3	1.11	0.97	1.26	0.94	1.24	0.90	1.18	0.84
L4	0.85	0.91	1.08	0.93	0.89	0.84		
L5	1.06	0.71	1.28	0.91	1.16	0.79		
CIRCUMFERENTIAL DISPLACEMENT VALIDATION (VERTEBRAE)								
Vertebra	*Right anterolateral aspect*		*Left anterolateral aspect*		*Pooled by specimen*		*Total*	
	slope	R^2	slope	R^2	slope	R^2	slope	R^2
L3	1.23	0.78	1.42	0.88	1.37	0.85	1.30	0.82
L4	1.78	0.83	1.15	0.83	1.31	0.79		
L5	1.16	0.76	1.15	0.96	1.16	0.84		

Strain validation

Longitudinal strains could be accurately predicted by pFEM. The frequency distribution of point-wise errors (shown as percentage of the DIC measured value in Figure 8) for longitudinal strains was centered in zero (median 0.6%, Wilcoxon signed rank test p=0.36), with a rather narrow expansion. Half of the predicted displacements were within 12.5% accuracy (interquartile range IQR = 25%), and the 95% percentile was within 27% accuracy.

Circumferential strain errors were instead biased towards pFEM overestimation, with median error of 39%, IQR of 59%, and around 10% of data over 100% error.

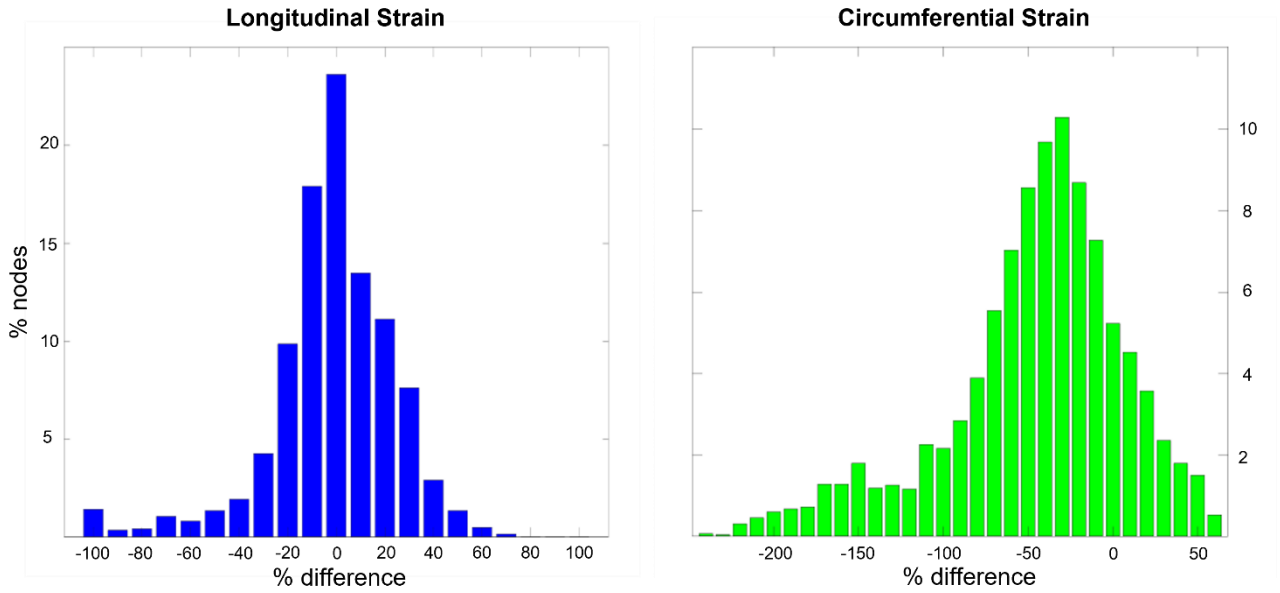

Figure 8: Frequency distribution plots of point-wise pFEM prediction errors in longitudinal (left) and circumferential (right) direction. Errors are shown in percentage of the DIC measured value ((DIC – pFEM)/100)/DIC, so that negative values indicate pFEM overestimation

Maps of point-wise relative strain errors trends revealed some spatial trends in pFEM accuracy (Figure 9). In general, the central region of each aspect (i.e. where the DIC image is focused) showed very low errors (close to zero even in most circumferential strain error maps). Higher errors were confined at image corners for longitudinal strains, while they extended also inwards for circumferential strains, highlighting pFEM overestimation.

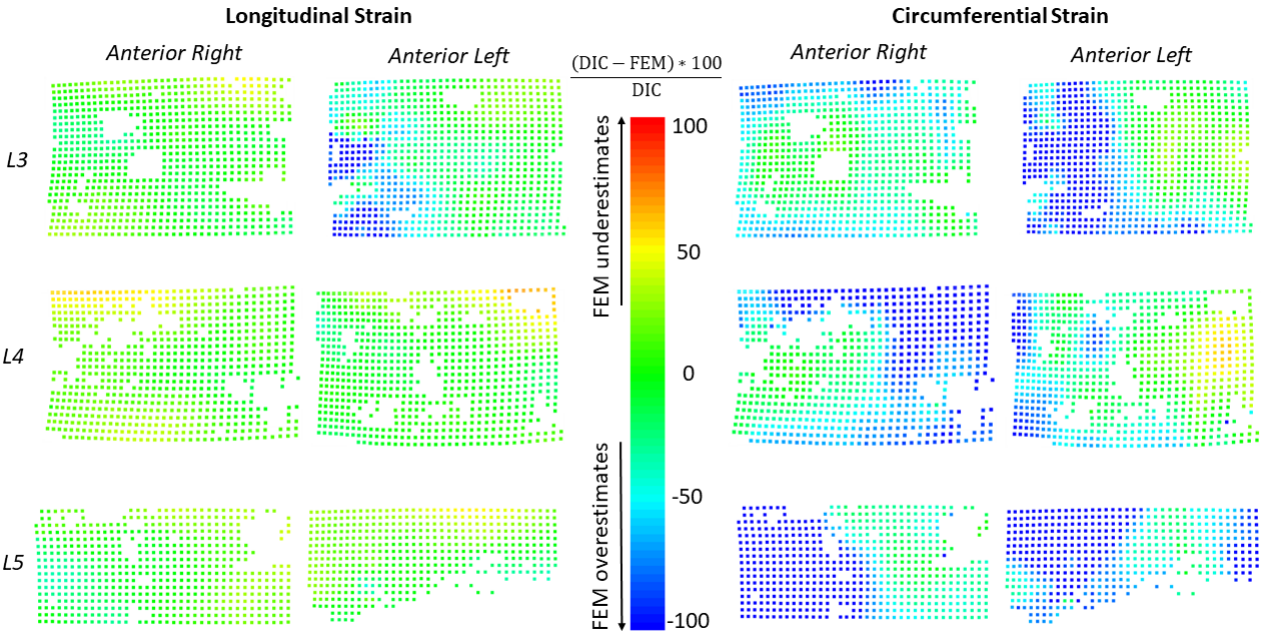

Figure 9: Accuracy maps of vertical (left) and circumferential (right) strain predictions, reporting percentage relative errors with respect to the experimental measurements.

4. DISCUSSION

In this study we presented and validated a new loading system designed to apply a homogeneous pressure field over the cranial vertebral endplate.

Effectiveness of the loading system

The effectiveness of the loading system was assessed by testing three pseudovertebrae and comparing the experimental measurements with theoretically calculated values, based on the assumption that a homogeneous specimen, irregular in shape but with vertical walls, undergoes homogeneous internal stress distribution, and therefore homogeneous longitudinal deformation distribution, when homogeneously loaded. The contact pressure distribution, measured at the caudal end/ceramic plate interface, and the longitudinal strain distribution, measured on three aspects of each pseudovertebra, proved the effectiveness of the loading system. Although closer to the theoretically calculated values, both mean contact pressure and mean longitudinal strain were underestimated (about -5% for both physical quantities). Different reasons explain these systematic biases. Mean pressure underestimation seems to be ascribed to unavoidable inaccuracies occurring during calibration of the pressure sensor array. The sensor was preliminary calibrated by applying a known load (-2.0 kN) through a UHMWPE cylinder. The total area of the activated squared sensors (1.9x1.9 mm) exceeded the cross-sectional area of the cylinder, therefore determining an underestimation of the reference pressure value. Edge effects, i.e. the activation of pressure sensors of the array closer to the cylinder edge that did not undergo any compressive load, further concurred to pressure underestimation. Strain underestimation, was, at least partly, due to measuring errors of DIC technique. Indeed, a systematic underestimation in longitudinal strain has been reported comparing strain gauge and DIC technique in measuring small-magnitude (<0.1%) homogeneous strain fields in ideal conditions, i.e. flat continuous specimen surface (Acciaioli et al., 2018). Our findings are consistent with that study also in terms of overestimation of the transversal strain. The out-of-plane displacements, which DIC systems measure with a lower accuracy (Schreier et al., 2009; Sutton et al., 2008), might have further noised the circumferential strain values. This additional bias seems to depend on whether the surface was convex (positive bias) or concave (negative bias) (Bornert et al., 2009; Del Rey Castillo et al., 2019). Therefore, the smaller the out-of-plane displacement (as it occurs in the central area of the monitored surface), the more accurate the DIC measurements (Murienne and Nguyen, 2016). An additional source of error is related to the flat preparation (by sanding) of the caudal end of the pseudovertebra. A slight sub-optimal contact at the caudal end/ceramic plate interface alters the strain distribution starting from the caudal end. Since the pseudovertebrae are short (they are machined to replicate the height of the vertebral body), any localized contact or sub-optimal contact at the caudal end/ceramic plate interface

respectively increase or decrease the longitudinal strain: the farther the contact conditions from the ideal contact, the greater the bias in the longitudinal strain (Jerabek et al., 2010). The applied procedure, designed to capture the variability in smoothing the lower end of the pseudovertebra, showed that the experimental percentage error, calculated for the single test repetition, fell in the range -17% ÷ 6% and -20% ÷ 29% for longitudinal and circumferential strains, respectively. These non-negligible deviations demonstrate the importance of caudal end/ceramic plate contact on the longitudinal strain levels, notwithstanding the exclusion of a 5 mm caudal strip from the monitored surfaces. Despite all these sources of experimental errors, the measured maximum differences among the three pseudovertebral aspects (30 μstrain) and the homogeneous pressure distribution (about 95% of the theoretically calculated value) measured at the caudal end/ceramic plate interface constitute experimental evidence of the effectiveness of the proposed loading system in loading homogeneously the cranial endplate.

Pilot study on human vertebrae

All the above reported observation about the experimental errors can be reasonably extended to the pilot study on human vertebral bodies. However, further inaccuracies in DIC measurements were there related to local irregularities and double curvatures of the vertebral walls, which determine non-ideal conditions for strain measurements (Acciaioli et al., 2020; Hassan, 2019). Indeed, the worst precision (random) errors were always measured on the posterior aspect of the vertebra, although always smaller than 0.4 μm and 80 μstrain for circumferential displacement and strain, respectively. These values were achieved using subsets of 36x36 pixels (i.e. about 0.40x0.40 mm), step of 36 pixels (i.e. no subset overlap) and 11x11 strain windows (i.e. about 4.36x4.36 mm), i.e. the best compromise between measurement accuracy and resolution, according to the approach proposed in previous reports for optimizing DIC measurements (Palanca et al., 2015; Pan et al., 2008; Wigger et al., 2018; Yaofeng and Pang, 2007). We could directly compare our experimental results only with Zeinali et al. (2010) where a rubber disk was used as interface to achieve "*pure compressive loading condition without creating any momentum during the test*", but surface displacements/strains were not measured. Comparisons with other loading systems are harder to attempt, although a common finding is that the human vertebral body under axial compression testing undergoes non-homogeneous deformation, irrespective of the loading system: through homogeneous pressure (as in our case), through acrylic molds embedding the endplates (Cristofolini et al., 2013; Gustafson et al., 2017a), or through intervertebral disks (Frei et al., 2002; Timothy M Jackman et al., 2016; Lu et al., 2013; Palanca et al., 2018; Shah et al., 1978). However, the main aim of this study was to experimentally achieve a homogeneous pressure distribution over the cranial endplate, which can be replicated in a clinically-feasible numerical model. This consistency

between the experimental and numerical boundary conditions cannot be fully achieved if the pressure distribution is not known (i.e. when the load is applied through the intervertebral disk or a rubber disk) or the full constraint of the endplate cannot be ensured (i.e. when the load is applied through acrylic molds embedding the endplates) due to resin shrinkage. A DVC approach can overcome this limitation (Costa et al., 2017) by providing accurate endplate displacements under load that can be used as boundary conditions in the model. However, such an approach (i) requires microCT imaging, and (ii) neglects the constitutive relationship. As the boundary conditions and the target validation parameter are the same physical quantity, i.e. displacements (or strains derived from displacements), the load necessary to determine the observed displacements remains uncertain (Costa et al., 2017). Here, a homogeneous pressure was applied to the cranial endplate (no assumption on endplate displacements) and surface displacements/strains were measured.

pFEM accuracy vs. DIC measurements

This study reports, for the first time to our knowledge, full-field pFEM validation results on human vertebral bodies for both displacements and strains in both longitudinal and circumferential directions. To our knowledge, no other studies than (Gustafson et al., 2017a) addressed DIC displacement validation on vertebral bodies. Recently, DIC was used to positively validate impact stiffness of the cervical vertebrae (Agostinho Hernandez et al., 2020) or FSU kinematics (Garavelli et al., 2022) but without including the prediction of strains in the vertebral body. We confirmed, for displacements in longitudinal direction, the good results reported by Gustafson et al., (2017a), by replicating their model in terms of density-elasticity relationship, although using different loading conditions. These results were achieved accurately aligning the DIC and pFEM reference systems, as recommended by Gustafson et al., (2017a).

In our study the validation was extended to longitudinal strains, which showed a null systematic error and a narrow scatter (Figure 8), mostly confined at the boundaries of the monitored surfaces (Figure 9). This extension was not possible for posterior vertebral aspects, which were not considered in Gustafson et al. (2017a). In longitudinal displacements, despite relatively good R^2 values, slopes differed substantially between specimens (Supplementary Material, Appendix C). In circumferential displacements, missing experimental data (structural discontinuities and curvature effects limit the application of DIC technique (Table 5) combined with weaknesses of pFEM (boundary identification) yielding lower correlation, apart from L5 where the DIC area coverage was higher. Due to elusive boundaries and inter-specimen variabilities of the venous plexus, microstructural insight would be likely needed to robustly approach vertebral posterior aspects.

In anterolateral aspect, however, a good accuracy was achieved also in circumferential displacements, despite the very small entity of the absolute values measured. When all

displacements were pooled together, they returned a very compact appearance of pFEM vs. DIC displacement data (Figure 7). The only apparent deviation in that plot came from the right anterolateral aspect of L4, where the maximum (unexpected) gradient in longitudinal displacements was measured. Overall, pFEM displacements were slightly overestimated, more steadily in circumferential than in longitudinal direction (Table 8). In addition to the already mentioned reduced accuracy in experimental data, this effect was possibly due to the pFEM approximation of the experimental caudal constraint.

pFEM overestimation of circumferential displacements was amplified in circumferential strain accuracy, with a consistent systematic overestimation (mean 39%), and a larger scatter in errors with respect to longitudinal strains (Figure 8). Circumferential strain overestimation may be partly attributed to the choice of the constitutive equation, which is not free from uncertainties: (i) Poisson's ratios are known to be difficult to measure in trabecular bone and were taken from microstructural simulations (Ulrich et al., 1999); (ii) there is a complete lack of mechanical data on vertebral cortical bone, which may exhibit peculiar behavior due to its thinness (vertebral walls) or microstructure (endplates, (McKay et al., 2020)) reflecting also in its cortical-specific density-elasticity relationships. The larger scatter in circumferential strain errors could also be related to lower DIC accuracy in measuring strains at the corners of the monitored surface. Indeed, almost all maps (Figure 9) showed good strain agreement in the central area of the monitored surface, where the surface morphology came closest to the ideal conditions.

Limitations

The sample size was small. The three vertebral bodies were excised from a single donor, neglecting the concept of functional spinal unit (FSU) as well as posterior vertebral elements. However, the main objective of this work was to assess the effectiveness of a new loading system to apply a homogeneous pressure over the endplate. The collected data constitute experimental evidence of the effectiveness of the proposed experimental model.

Deviations from purely compressive loads, which are indeed present in motor activities (Rohlmann et al., 2014), were not considered. In our view, the accuracy of pFEM predictions should first be assessed for the simplest loading condition, then extended to more physiological ones, eventually including posterior elements to capture the actual sharing of load between spinal structures (Azari et al., 2018). However, this would mean performing multiaxial testing on multi-tissue specimens, and adding kinematic components, non-linear materials and multiple contact interfaces to the pFEM, which was out of the compass of this study.

The structural integrity of vertebral bodies was caudally interrupted, potentially weakening them. Also, any prevalent wedge angle or deformity, which may by itself be a risk factor (Lunt et al.,

2003; Zhao et al., 2022) was neglected. However, this study did not measure the compressive strength of vertebral body. This was an unavoidable limitation to complete the validation of the experimental loading system by measuring the pressure distribution at the lower flat end.

In terms of prospective applicability, the pFEM is not validated to reproduce fully physiological loading conditions. However, it can account for endplate compliance. Additionally, it is clinically feasible because it does not require knowledge of endplate displacements (currently possible only by DVC, i.e. not in vivo). Thus, it may be appropriate to capture changes in strain fields under load, as made evident by (Hussein et al., 2018), although we still neglect microstructure as it cannot be recovered from clinical images yet.

In summary, (i) we proposed a new vertebral loading system that applies well controlled boundary conditions, loading the cranial endplate with a uniform pressure as proven by measurements on homogeneous pseudovertebrae; (ii) we reported for the first time full field DIC measurements of longitudinal and circumferential displacements and strain in human vertebrae, with very high precision; (iii) we confirmed that control of experimental boundary conditions is key to a good FE validation, as (iv) we obtained a good accuracy in the pFEM validation of displacements and longitudinal strains, although circumferential strains were overestimated, and in posterior aspects DIC-FE comparisons were hindered by anatomical features (curvature, venous plexus) influencing both DIC and pFEM robustness. These new methods may be applied to study how physiological and pathologic conditions influence the ability of vertebral endplates to sustain loads.

Acknowledgements

The authors would like to thank Alice Acciaioli and Roberta Fognani for their help in carrying out the tests, Nicola Vanella and Gianluigi Crimi for the help with software devclopment/fixing, and Luigi Lena for the illustrations.

CRediT authorship contribution statement

Conceptualization: Massimiliano Baleani, Enrico Schileo; Methodology: Massimiliano Baleani, Paolo Erani, Fulvia Taddei, Enrico Schileo; Software: Giulia Rota, Matteo Berni, Fulvia Taddei, Enrico Schileo, Giulia Fraterrigo; Validation: All authors; Formal analysis: Giulia Fraterrigo, Paolo Erani, Giulia Rota, Matteo Berni; Investigation; Giulia Fraterrigo, Paolo Erani, Giulia Rota, Matteo Berni, Enrico Schileo; Resources: Massimiliano Baleani, Fulvia Taddei; Data curation; Giulia Fraterrigo, Paolo Erani, Giulia Rota, Matteo Berni; Writing - original draft; Massimiliano Baleani, Enrico Schileo, Giulia Fraterrigo; Writing - review & editing. All authors; Visualization: Giulia Fraterrigo, Paolo Erani, Giulia Rota; Supervision: Massimiliano Baleani, Enrico Schileo; Project administration: Massimiliano Baleani, Fulvia Taddei, Enrico Schileo; Funding acquisition: Massimiliano Baleani, Fulvia Taddei, Enrico Schileo.

Funding

This research was supported by the Italian Ministry of Health, grant number RF-Grant: RF-2016-02364359, project title: qSINS - Quantitative revision of the Spinal Instability Neoplastic Score including CT-based assessment of spinal condition and finite element modeling of vertebral strength. A prospective clinical study.

Declaration of interests

The authors declare that they have no known competing financial interests or personal relationships that could have appeared to influence the work reported in this paper.

Data availability

A comprehensive report and analysis of the data collected are available in the Appendices. Raw data will be made available on request.

References

Acciaioli, A., Falco, L., Baleani, M., 2020. Measurement of apparent mechanical properties of trabecular bone tissue: Accuracy and limitation of digital image correlation technique. Journal of the Mechanical Behavior of Biomedical Materials 103, 103542. https://doi.org/10.1016/j.jmbbm.2019.103542

Acciaioli, A., Lionello, G., Baleani, M., 2018. Experimentally Achievable Accuracy Using a Digital Image Correlation Technique in measuring Small-Magnitude (<0.1%) Homogeneous Strain Fields. Materials 11, 751. https://doi.org/10.3390/ma11050751

Agostinho Hernandez, B., Gill, H.S., Gheduzzi, S., 2020. A Novel Modelling Methodology Which Predicts the Structural Behaviour of Vertebral Bodies under Axial Impact Loading: A Finite Element and DIC Study. Materials 13, 4262. https://doi.org/10.3390/ma13194262

Ayturk, U.M., Puttlitz, C.M., 2011. Parametric convergence sensitivity and validation of a finite element model of the human lumbar spine. Computer Methods in Biomechanics and Biomedical Engineering 14, 695–705. https://doi.org/10.1080/10255842.2010.493517

Azari, F., Arjmand, N., Shirazi-Adl, A., Rahimi-Moghaddam, T., 2018. A combined passive and active musculoskeletal model study to estimate L4-L5 load sharing. Journal of Biomechanics 70, 157–165. https://doi.org/10.1016/j.jbiomech.2017.04.026

Banse, X., Devogelaer, J.P., Munting, E., Delloye, C., Cornu, O., Grynpas, M., 2001. Inhomogeneity of human vertebral cancellous bone: systematic density and structure patterns inside the vertebral body. Bone 28, 563–571. https://doi.org/10.1016/S8756-3282(01)00425-2

Bornert, M., Brémand, F., Doumalin, P., Dupré, J.C., Fazzini, M., Grédiac, M., Hild, F., Mistou, S., Molimard, J., Orteu, J., Robert, L., Surrel, Y., Vcher, P., Wattrisse, B., 2009. Assessment of digital image correlation measurement errors: methodology and results. Experimental Mechanics, vol. 49 (n° 3). pp. 353-370. http://dx.doi.org/10.1007/s11340 008-9204-7

Bruno, A.G., Bouxsein, M.L., Anderson, D.E., 2015. Development and Validation of a Musculoskeletal Model of the Fully Articulated Thoracolumbar Spine and Rib Cage. Journal of Biomechanical Engineering 137(8): 081003. https://doi.org/10.1115/1.4030408

Bruno, A.G., Burkhart, K., Allaire, B., Anderson, D.E., Bouxsein, M.L., 2017. Spinal Loading Patterns from Biomechanical Modeling Explain the High Incidence of Vertebral Fractures in

760 the Thoracolumbar Region. Journal of Bone and Mineral Research 32, 1282–1290.
761 https://doi.org/10.1002/jbmr.3113

762 Buckley, J.M., Loo, K., Motherway, J., 2007. Comparison of quantitative computed tomography-
763 based measures in predicting vertebral compressive strength. Bone 40, 767–774.
764 https://doi.org/10.1016/j.bone.2006.10.025

765 Chevalier, Y., Charlebois, M., Pahr, D., Varga, P., Heini, P., Schneider, E., Zysset, P., 2008. A
766 patient-specific finite element methodology to predict damage accumulation in vertebral
767 bodies under axial compression, sagittal flexion and combined loads. Computer Methods in
768 Biomechanics and Biomedical Engineering 11, 477–487.
769 https://doi.org/10.1080/10255840802078022

770 Choisne, J., Valiadis, J.M., Travert, C., Kolta, S., Roux, C., Skalli, W., 2015. Vertebral strength
771 prediction under anterior compressive force using a finite element model for osteoporosis
772 assessment. Computer Methods in Biomechanics and Biomedical Engineering 18, 1900–
773 1901. https://doi.org/10.1080/10255842.2015.1069562

774 Cignoni, P., Callieri, M., Corsini, M., Dellepiane, M., Ganovelli, F., Ranzuglia, G., 2008.
775 MeshLab: an Open-Source Mesh Processing Tool. Eurographics Italian Chapter Conference
776 (2008) Proceedings (V. Scarano, R. De Chiara, and U. Erra Editors):129-136.
777 DOI:10.2312/LocalChapterEvents/ItalChap/ItalianChapConf2008/129-136

778 Costa, M.C., Tozzi, G., Cristofolini, L., Danesi, V., Viceconti, M., Dall'Ara, E., 2017. Micro Finite
779 Element models of the vertebral body: Validation of local displacement predictions. PLoS
780 ONE 12, e0180151. https://doi.org/10.1371/journal.pone.0180151

781 Crawford, R.P., Cann, C.E., Keaveny, T.M., 2003. Finite element models predict in vitro vertebral
782 body compressive strength better than quantitative computed tomography. Bone 33, 744–
783 750. https://doi.org/10.1016/S8756-3282(03)00210-2

784 Cristofolini, L., Brandolini, N., Danesi, V., Juszczyk, M.M., Erani, P., Viceconti, M., 2013. Strain
785 distribution in the lumbar vertebrae under different loading configurations. The Spine
786 Journal 13, 1281–1292. https://doi.org/10.1016/j.spinee.2013.06.014

787 Dall'Ara, E., Schmidt, R., Pahr, D., Varga, P., Chevalier, Y., Patsch, J., Kainberger, F., Zysset, P.,
788 2010. A nonlinear finite element model validation study based on a novel experimental
789 technique for inducing anterior wedge-shape fractures in human vertebral bodies in vitro. J
790 Biomech 43, 2374–2380. https://doi.org/10.1016/j.jbiomech.2010.04.023

Del Rey Castillo, E., Allen, T., Henry, R., Griffith, M., Ingham, J., 2019. Digital image correlation (DIC) for measurement of strains and displacements in coarse, low volume-fraction FRP composites used in civil infrastructure. Composite Structures 212, 43–57. https://doi.org/10.1016/j.compstruct.2019.01.024

Dong, X.N., Guo, X.E., 2004. The dependence of transversely isotropic elasticity of human femoral cortical bone on porosity. Journal of Biomechanics 37, 1281–1287. https://doi.org/10.1016/j.jbiomech.2003.12.011

Dong, X.N., Guo, X.E., 2006. Prediction of Cortical Bone Elastic Constants by a Two-Level Micromechanical Model Using a Generalized Self-Consistent Method. Journal of Biomechanical Engineering 128, 309–316. https://doi.org/10.1115/1.2187039

Eswaran, S.K., Gupta, A., Adams, M.F., Keaveny, T.M., 2006. Cortical and trabecular load sharing in the human vertebral body. J Bone Miner Res 21, 307–314. https://doi.org/10.1359/jbmr.2006.21.2.307

Frei, H., Oxland, T.R., Nolte, L.-P., 2002. Thoracolumbar spine mechanics contrasted under compression and shear loading. J. Orthop. Res. 20, 1333–1338. https://doi.org/10.1016/S0736-0266(02)00058-X

Garavelli, C., Curreli, C., Palanca, M., Aldieri, A., Cristofolini, L., Viceconti, M., 2022. Experimental validation of a subject-specific finite element model of lumbar spine segment using digital image correlation. PLoS ONE 17, e0272529. https://doi.org/10.1371/journal.pone.0272529

Grassi, L., Väänänen, S.P., Amin Yavari, S., Weinans, H., Jurvelin, J.S., Zadpoor, A.A., Isaksson, H., 2013. Experimental validation of finite element model for proximal composite femur using optical measurements. Journal of the Mechanical Behavior of Biomedical Materials 21, 86–94. https://doi.org/10.1016/j.jmbbm.2013.02.006

Groenen, K.H.J., Bitter, T., van Veluwen, T.C.G., van der Linden, Y.M., Verdonschot, N., Tanck, E., Janssen, D., 2018. Case-specific non-linear finite element models to predict failure behavior in two functional spinal units. Journal of Orthopaedic Research. https://doi.org/10.1002/jor.24117

Gustafson, H.M., Cripton, P.A., Ferguson, S.J., Helgason, B., 2017a. Comparison of specimen-specific vertebral body finite element models with experimental digital image correlation measurements. Journal of the Mechanical Behavior of Biomedical Materials 65, 801–807. https://doi.org/10.1016/j.jmbbm.2016.10.002

Gustafson, H.M., Melnyk, A.D., Siegmund, G.P., Cripton, P.A., 2017b. Damage Identification on Vertebral Bodies During Compressive Loading Using Digital Image Correlation. Spine 42, E1289–E1296. https://doi.org/10.1097/BRS.0000000000002156

Hassan, G.M., 2019. Digital Image Correlation for discontinuous displacement measurement using subset segmentation. Optics and Lasers in Engineering 115, 208–216. https://doi.org/10.1016/j.optlaseng.2018.12.003

Hussein, A.I., Louzeiro, D.T., Unnikrishnan, G.U., Morgan, E.F., 2018. Differences in Trabecular Microarchitecture and Simplified Boundary Conditions Limit the Accuracy of Quantitative Computed Tomography-Based Finite Element Models of Vertebral Failure. Journal of Biomechanical Engineering 140, 021004. https://doi.org/10.1115/1.4038609

Imai, K., Ohnishi, I., Bessho, M., Nakamura, K., 2006. Nonlinear Finite Element Model Predicts Vertebral Bone Strength and Fracture Site: Spine 31, 1789–1794. https://doi.org/10.1097/01.brs.0000225993.57349.df

Jackman, T.M., DelMonaco, A.M., Morgan, E.F., 2016. Accuracy of finite element analyses of CT scans in predictions of vertebral failure patterns under axial compression and anterior flexion. Journal of Biomechanics 49, 267–275. https://doi.org/10.1016/j.jbiomech.2015.12.004

Jackman, T.M., Hussein, A.I., Adams, A.M., Makhnejia, K.K., Morgan, E.F., 2014. Endplate deflection is a defining feature of vertebral fracture and is associated with properties of the underlying trabecular bone. Journal of Orthopaedic Research 32, 880–886. https://doi.org/10.1002/jor.22620

Jackman, T.M, Hussein, A.I., Curtiss, C., Fein, P.M., Camp, A., De Barros, L., Morgan, E.F., 2016. Quantitative, 3D Visualization of the Initiation and Progression of Vertebral Fractures Under Compression and Anterior Flexion. Journal of Bone and Mineral Research 31, 777–788. https://doi.org/10.1002/jbmr.2749

Jerabek, M., Major, Z., Lang, R.W., 2010. Uniaxial compression testing of polymeric materials. Polymer Testing 29, 302–309. https://doi.org/10.1016/j.polymertesting.2009.12.003

Langrana, N.A., Kale, S.P., Edwards, W.T., Lee, C.K., Kopacz, K.J., 2006. Measurement and analyses of the effects of adjacent end plate curvatures on vertebral stresses. The Spine Journal 6, 267–278. https://doi.org/10.1016/j.spinee.2005.09.008

Lionello, G., Cristofolini, L., 2014. A practical approach to optimizing the preparation of speckle patterns for digital-image correlation. Meas. Sci. Technol. 25, 107001. https://doi.org/10.1088/0957-0233/25/10/107001

Lu, Y., Rosenau, E., Paetzold, H., Klein, A., Puschel, K., Morlock, M.M., Huber, G., 2013. Strain changes on the cortical shell of vertebral bodies due to spine ageing: a parametric study using a finite element model evaluated by strain measurements. Proc Inst Mech Eng H 227, 1265–1274. https://doi.org/10.1177/0954411913501293

Lunt, M., O'Neill, T.W., Felsenberg, D., Reeve, J., Kanis, J.A., Cooper, C., Silman, A.J., 2003. Characteristics of a prevalent vertebral deformity predict subsequent vertebral fracture: results from the European Prospective Osteoporosis Study (EPOS). Bone 33, 505–513. https://doi.org/10.1016/S8756-3282(03)00248-5

Maquer, G., Schwiedrzik, J., Zysset, P.K., 2014. Embedding of human vertebral bodies leads to higher ultimate load and altered damage localisation under axial compression. Comput Methods Biomech Biomed Engin 17, 1311–1322. https://doi.org/10.1080/10255842.2012.744400

McKay, M., Jackman, T.M., Hussein, A.I., Guermazi, A., Liu, J., Morgan, E.F., 2020. Association of vertebral endplate microstructure with bone strength in men and women. Bone 131, 115147. https://doi.org/10.1016/j.bone.2019.115147

Mirzaei, M., Zeinali, A., Razmjoo, A., Nazemi, M., 2009. On prediction of the strength levels and failure patterns of human vertebrae using quantitative computed tomography (QCT)-based finite element method. Journal of Biomechanics 42, 1584–1591. https://doi.org/10.1016/j.jbiomech.2009.04.042

Murienne, B.J., Nguyen, T.D., 2016. A comparison of 2D and 3D digital image correlation for a membrane under inflation. Optics and Lasers in Engineering 77, 92–99. https://doi.org/10.1016/j.optlaseng.2015.07.013

Ouyang, J., Yang, G., Wu, W., Zhu, Q., Zhong, S., 1997. Biomechanical characteristics of human trabecular bone. Clin. Biomech. 12, 522–524. https://doi.org/10.1016/S0268-0033(97)00035-1

Palanca, M., Barbanti-Bròdano, G., Cristofolini, L., 2018. The Size of Simulated Lytic Metastases Affects the Strain Distribution on the Anterior Surface of the Vertebra. Journal of Biomechanical Engineering 140, 111005. https://doi.org/10.1115/1.4040587

884 Palanca, M., Brugo, T.M., Cristofolini, L., 2015. Use of Digital Image Correlation to Investigate the
885 Biomechanics of the Vertebra. J. Mech. Med. Biol. 15, 1540004.
886 https://doi.org/10.1142/S0219519415400047

887 Palanca, M., De Donno, G., Dall'Ara, E., 2021. A novel approach to evaluate the effects of artificial
888 bone focal lesion on the three-dimensional strain distributions within the vertebral body.
889 PLoS ONE 16, e0251873. https://doi.org/10.1371/journal.pone.0251873

890 Pan, B., Xie, H., Wang, Zhaoyang, Qian, K., Wang, Zhiyong, 2008. Study on subset size selection
891 in digital image correlation for speckle patterns. Opt. Express 16, 7037.
892 https://doi.org/10.1364/OE.16.007037

893 Panjabi, M.M., Goel, V., Oxland, T., Takata, K., Duranceau, J., Krag, M., Price, M., 1992. Human
894 lumbar vertebrae. Quantitative three-dimensional anatomy. Spine 17, 299–306. DOI:
895 10.1097/00007632-199203000-00010

896 Rohlmann, A., Dreischarf, M., Zander, T., Graichen, F., Bergmann, G., 2014. Loads on a vertebral
897 body replacement during locomotion measured in vivo. Gait & Posture 39, 750–755.
898 https://doi.org/10.1016/j.gaitpost.2013.10.010

899 Rohlmann, A., Zander, T., Graichen, F., Bergmann, G., 2013. Lifting up and laying down a weight
900 causes high spinal loads. Journal of Biomechanics 46, 511–514.
901 https://doi.org/10.1016/j.jbiomech.2012.10.022

902 Schileo, E., Dall'Ara, E., Taddei, F., Malandrino, A., Schotkamp, T., Baleani, M., Viceconti, M.,
903 2008. An accurate estimation of bone density improves the accuracy of subject-specific
904 finite element models. Journal of Biomechanics 41, 2483–2491.
905 https://doi.org/10.1016/j.jbiomech.2008.05.017

906 Schileo, E., Pitocchi, J., Falcinelli, C., Taddei, F., 2020. Cortical bone mapping improves finite
907 element strain prediction accuracy at the proximal femur. Bone 136, 115348.
908 https://doi.org/10.1016/j.bone.2020.115348

909 Schreier, H., Orteu, J.-J., Sutton, M.A., 2009. Image Correlation for Shape, Motion and
910 Deformation Measurements. Springer US, Boston, MA. https://doi.org/10.1007/978-0-387-
911 78747-3

912 Shah, J., Hampson, W., Jayson, M., 1978. The distribution of surface strain in the cadaveric lumbar
913 spine. The Journal of Bone and Joint Surgery. British volume 60-B, 246–251.
914 https://doi.org/10.1302/0301-620X.60B2.659474

Sherazi, T.A., 2014. Ultrahigh Molecular Weight Polyethylene, in: Drioli, E., Giorno, L. (Eds.), Encyclopedia of Membranes. Springer Berlin Heidelberg, Berlin, Heidelberg, pp. 1–2. https://doi.org/10.1007/978-3-642-40872-4_591-2

Sutton, M.A., Yan, J.H., Tiwari, V., Schreier, H.W., Orteu, J.J., 2008. The effect of out-of-plane motion on 2D and 3D digital image correlation measurements. Optics and Lasers in Engineering 46, 746–757. https://doi.org/10.1016/j.optlaseng.2008.05.005

Treece, G.M., Gee, A.H., 2015. Independent measurement of femoral cortical thickness and cortical bone density using clinical CT. Medical Image Analysis 20, 249–264. https://doi.org/10.1016/j.media.2014.11.012

Ulrich, D., van Rietbergen, B., Laib, A., Rüegsegger, P., 1999. The ability of three-dimensional structural indices to reflect mechanical aspects of trabecular bone. Bone 25, 55–60. https://doi.org/10.1016/S8756-3282(99)00098-8

Whyne, C.M., Hu, S.S., Lotz, J.C., 2003. Burst Fracture in the Metastatically Involved Spine: Development, Validation, and Parametric Analysis of a Three-Dimensional Poroelastic Finite-Element Model. Spine 28, 652–660. https://doi.org/10.1097/01.BRS.0000051910.97211.BA

Wigger, T., Lupton, C., Tong, J., 2018. A parametric study of DIC measurement uncertainties on cracked metals. Strain 54, e12291. https://doi.org/10.1111/str.12291

Yaofeng, S., Pang, J.H.L., 2007. Study of optimal subset size in digital image correlation of speckle pattern images. Optics and Lasers in Engineering 45, 967–974. https://doi.org/10.1016/j.optlaseng.2007.01.012

Zeinali, A., Hashemi, B., Akhlaghpoor, S., 2010. Noninvasive prediction of vertebral body compressive strength using nonlinear finite element method and an image based technique. Phys Med 26. https://doi.org/10.1016/j.ejmp.2009.08.002

Zhao, C., Liu, X., Wang, Y., Guo, J., Han, S., Zhang, H., Chen, M., Zhou, C., Ma, X., 2022. The effects of biomechanical factors on adjacent vertebral compression fractures after percutaneous kyphoplasty: a propensity score matching analysis. Osteoporos Int 33, 1795–1806. https://doi.org/10.1007/s00198-022-06428-5

Zhou, P., 2001. Subpixel displacement and deformation gradient measurement using digital image/speckle correlation (DISC). Opt. Eng 40, 1613. https://doi.org/10.1117/1.1387992